SURFACE SCIENCE

Synthesis and characterization of low-dimensional N-heterocyclic carbene lattices

Boyu Qie[1,2]†, Ziyi Wang[3,4,2]†, Jingwei Jiang[3,4]†, Zisheng Zhang[5], Peter H. Jacobse[3,4], Jiaming Lu[3], Xinheng Li[3], Fujia Liu[1], Anastassia N. Alexandrova[5,6,7], Steven G. Louie[3,4]*, Michael F. Crommie[3,4,2]*, Felix R. Fischer[1,4,2,8]*

The covalent interaction of N-heterocyclic carbenes (NHCs) with transition metal atoms gives rise to distinctive frontier molecular orbitals (FMOs). These emergent electronic states have spurred the widespread adoption of NHC ligands in chemical catalysis and functional materials. Although formation of carbene-metal complexes in self-assembled monolayers on surfaces has been explored, design and electronic structure characterization of extended low-dimensional NHC-metal lattices remains elusive. Here we demonstrate a modular approach to engineering one-dimensional (1D) metal-organic chains and two-dimensional (2D) Kagome lattices using the FMOs of NHC–Au–NHC junctions to create low-dimensional molecular networks exhibiting intrinsic metallicity. Scanning tunneling spectroscopy and first-principles density functional theory reveal the contribution of C–Au–C π-bonding states to dispersive bands that imbue 1D- and 2D-NHC lattices with exceptionally small work functions.

The singlet ground state of N-heterocyclic carbenes (NHCs) is characterized by the interaction of two N atoms adjacent to the carbene C atom. The stabilizing resonance between the nitrogen lone pairs and the vacant p_z orbital of a carbene C atom competes with the electrostatic effect of the polarized C–N σ bonds (1). This curious electronic structure has allowed NHCs to be used as organic ligands in diverse fields ranging from homogeneous and heterogeneous catalysis to supramolecular and polymer materials chemistry (2, 3). The interaction of NHCs with transition metals creates covalent metal–carbene bonding arrangements that retain singlet carbene character and give rise to frontier orbitals of unusual symmetry (4, 5).

Here we demonstrate a general approach for designing and fabricating extended, low-dimensional NHC-metal frameworks, including a one-dimensional (1D) chain and a two-dimensional (2D) Kagome lattice, based on the carbon-gold-carbon (C–Au–C) π-bonding states of NHC–Au–NHC junctions (Fig. 1, F and G). The in situ, on-surface synthesis of periodic structures was confirmed by real-space bond-resolved scanning tunneling microscopy (BRSTM) imaging. Scanning tunneling spectroscopy (STS) and first-principles theoretical modeling were used to determine the contribution of frontier orbitals to the electronic structure of these newly created low-dimensional materials.

We found that the singly occupied molecular orbital of NHC–Au–NHC junctions contributed to the intrinsic metallic bands of extended NHC-metal lattices and imbued these structures with exceptionally low work functions. A substantial charge transfer between the metal-organic framework (MOF) and the supporting gold substrate resulted in the observation of large-gapped semiconducting band structures. These results offer new possibilities for the design and synthesis of NHC-based MOFs with tailored electronic properties through the engineering of their frontier orbitals, with potential application in nanoelectronics and spin physics.

Design of 1D and 2D NHC–Au lattices

To understand the electronic properties of low-dimensional materials constructed from NHC–metal–NHC junctions, we considered

[1]Department of Chemistry, University of California, Berkeley, Berkeley, CA 94720, USA. [2]Kavli Energy NanoScience Institute at the University of California, Berkeley, and the Lawrence Berkeley National Laboratory, Berkeley, CA 94720, USA. [3]Department of Physics, University of California, Berkeley, Berkeley, CA 94720, USA. [4]Materials Sciences Division, Lawrence Berkeley National Laboratory, Berkeley, CA 94720, USA. [5]Department of Chemistry and Biochemistry, University of California, Los Angeles, Los Angeles, CA 90095, USA. [6]Department of Materials Science and Engineering, University of California, Los Angeles, Los Angeles, CA 90095, USA. [7]California NanoSystems Institute, University of California, Los Angeles, Los Angeles, CA 90095, USA. [8]Bakar Institute of Digital Materials for the Planet, Division of Computing, Data Science, and Society, University of California, Berkeley, Berkeley, CA 94720, USA.
*Corresponding author. Email: ffischer@berkeley.edu (F.R.F.); crommie@berkeley.edu (M.F.C.); sglouie@berkeley.edu (S.G.L.)
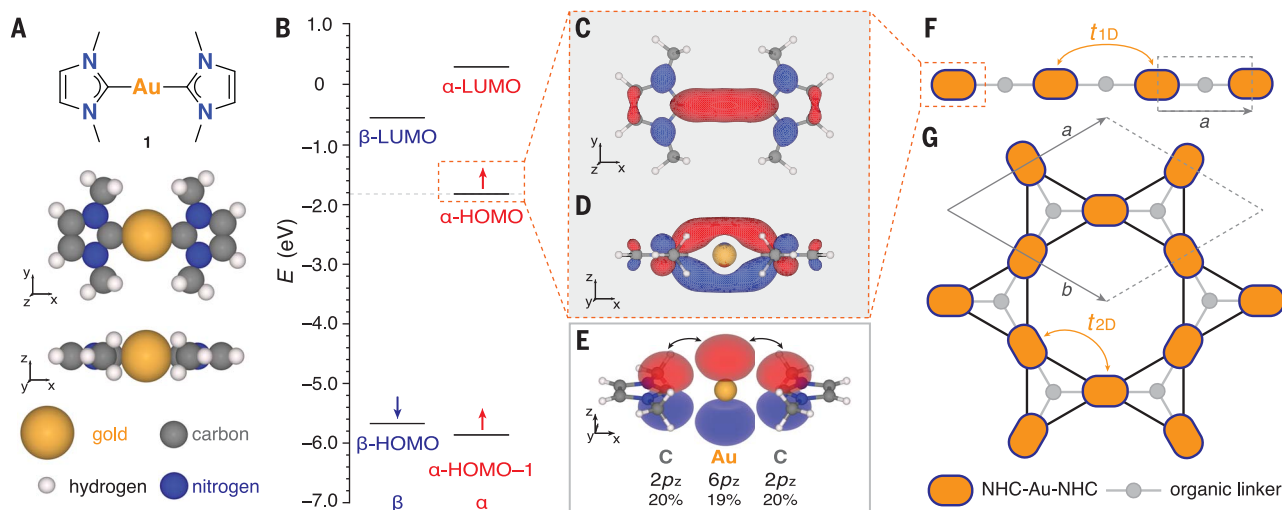†These authors contributed equally to this work.

Fig. 1. Frontier orbital energies for NHC–Au lattices. (**A**) Molecular model of a discrete NHC–Au–NHC complex 1. (**B**) Unrestricted DFT calculation showing the frontier molecular orbitals of 1 in isolation at charge neutrality. (**C** and **D**) Top-down and side-view projection of the DFT-LDA calculated wave function isosurface for the NHC–Au–NHC SOMO (α-HOMO) shows the three-center one-electron π bond shared between the Au atom and the two NHC ligands (red and blue colors represent phase). (**E**) Schematic representation of the pre-orthogonal natural atomic orbital (PNAO) contributions of the Au $6p_z$ and C $2p_z$ orbitals to the C–Au–C π bonding the SOMO. (**F**) Schematic representation of hopping (t) between NHC–Au–NHC junctions inside a 1D NHC-metal chain (1D-NHCAuC) and (**G**) a 2D NHC-metal Kagome lattice (2D-NHCAuKL).

the frontier molecular orbitals (FMOs) in the NHC–Au–NHC dimer bis(1,3-dimethyl-2,3-dihydro-1H-imidazol-2-yl) gold (1; Fig. 1A). Gold was selected as the metal center because of its electron configuration of [Xe]4f^{14}5d^{10}6s^{1}, which gives rise to a singly occupied state upon binding two NHC carbenes to Au^{0}. The central Au atom forms a linear complex with two coplanar NHC carbenes that serves as a linker element to span 1D or 2D lattices in the plane of NHC–Au–NHC junctions (Fig. 1, F and G).

Unrestricted density functional theory (DFT) calculations revealed the FMOs of dimer 1 (Fig. 1B). The highest occupied molecular orbital of the α electron (α-HOMO) is a singly occupied molecular orbital (SOMO) separated by a sizable gap (~4 eV) from the nearest occupied states, the β-HOMO and α-HOMO−1. The wave function of the α-HOMO (Fig. 1, C and D) is dominated by a linear three-center π bond shared between the Au atom and the p$_z$ orbitals of the two adjacent NHC C atoms. Natural bonding orbital analysis provided the natural atomic orbital (NAO) composition of the C–Au–C π bonding in the SOMO (6–8): The Au 6p$_z$ NAO contributes 19%, and the two C 2p$_z$ NAOs each contribute 20% (Fig. 1E shows the pre-orthogonal NAO wave functions). The low-lying β-HOMO and α-HOMO−1 states have Au 5d$_{xz}$ NAO character as well as some contribution from the NHC π system and place a node on the Au atom (fig. S1). The even-lower β-HOMO−1 and α-HOMO−2 states are almost exclusively centered on the Au atom and exhibit 42% 6s, 30% 5d$_{x^2-y^2}$, and 15% 5d$_{z^2}$ NAO from Au (fig. S1). The NAO contributions as well as the energetic and spatial isolation of the frontier SOMO orbital (α-HOMO) are conducive to the engineering of electronic structures for low-dimensional lattices constructed from NHC–Au–NHC junctions.

We herein focus on a pair of simple 1D and 2D extended NHC–Au lattices. The isolated frontier SOMO of 1 allowed us to approximate the eigenstate localized on the C–Au–C π bond as an isolated low-energy mode centered on the NHC–Au–NHC junction. Application of a simple electron hopping model to a periodic lattice of such junctions enabled the construction of an elementary low-energy effective nearest-neighbor tight-binding model that described the resultant electronic bands

$$H = -t_{1D(2D)} \sum_{\langle ij \rangle} c_i^\dagger c_j + \varepsilon \sum_i c_i^\dagger c_i$$

where $t_{1D(2D)}$ is the hopping parameter between adjacent localized low-energy modes for a 1D (2D) structure, ε is the on-site energy, and $c_i^\dagger$ and c_i are creation and annihilation operators for electrons at site i, respectively. The application of this model to a 1D lattice is illustrated in Fig. 1F and shows electron hopping between the C–Au–C SOMO states on the NHC–
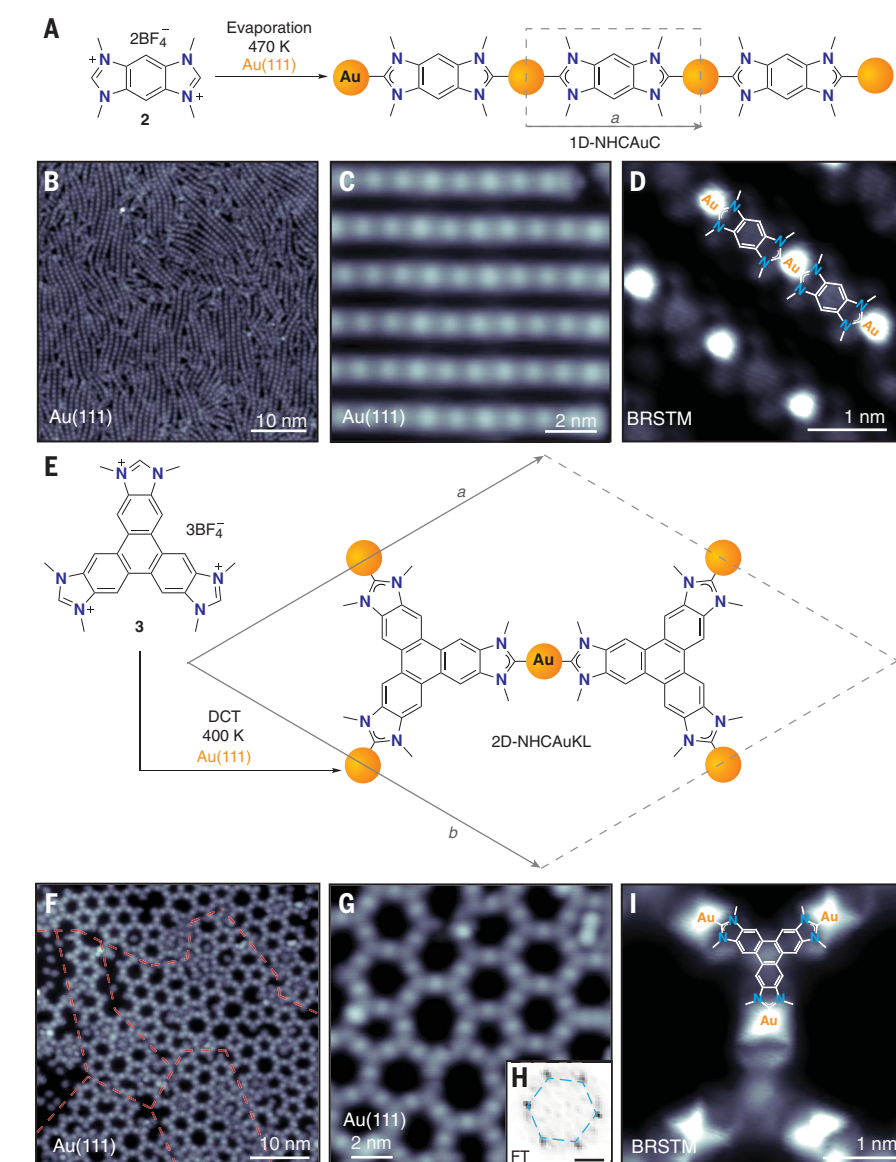

Fig. 2. Bottom-up synthesis of 1D-NHCAuC and 2D-NHCAuKL. (**A**) Schematic representation of the surface-mediated in situ synthesis of 1D-NHCAuC. (**B**) STM topographic image of 1D-NHCAuC on Au(111) [sample voltage bias (V_s) = −1800 mV, current setpoint (I_t) = 50 pA]. (**C**) Close-up STM topographic image of the 1D-NHCAuC on Au(111) (V_s = −1200 mV, I_t = 50 pA). (**D**) Constant-height BRSTM image of 1D-NHCAuC showing the formation of carbene bonds between phenyl-NHC ligands and Au atoms [V_s = 5 mV, modulation voltage (V_{ac}) = 30 mV, modulation frequency (f) = 533 Hz, CO-functionalized tip]. (**E**) Schematic representation of the surface-mediated in situ synthesis strategy for 2D-NHCAuKL. (**F**) STM topographic image of 2D-NHCAuKL on Au(111) (V_s = −1200 mV, I_t = 50 pA). (**G**) Close-up STM topographic image of the 2D-NHCAuKLs on Au(111) (V_s = −200 mV, I_t = 100 pA). (**H**) Fourier transform of the image shown in (G). The expected reciprocal unit vectors of 2D-NHCAuKLs are connected by blue dashed lines (scale bar: 0.5 nm^{-1}). (**I**) Constant-height BRSTM image of 2D-NHCAuKL showing the formation of carbene bonds between triphenylene-NHC ligands and Au atoms (V_s = −10 mV, V_{ac} = 30 mV, f = 533 Hz, CO-functionalized tip). All STM experiments were performed at T = 4 K.

Au–NHC junctions within a 1D NHC-gold chain (1D-NHCAuC). Here the organic linkers are depicted as gray circles, and NHC–Au–NHC junctions are shown as orange rounded rectangles.

Whereas a symmetric hopping parameter t_{1D} across all zero-mode states gives rise to a half-filled metallic band, a Peierls distortion could open a bandgap in the electronic struc-

ture of 1D-NHCAuC (9). Similar concepts can be extended to 2D structures, as shown by the electron hopping model of a 2D NHC-gold Kagome lattice (2D-NHCAuKL) in Fig. 1G. In this 2D network, the NHC–Au–NHC junctions serve as the hopping sites (orange) of a Kagome lattice, whereas the threefold organic linkers (gray) form the backbone of a honeycomb
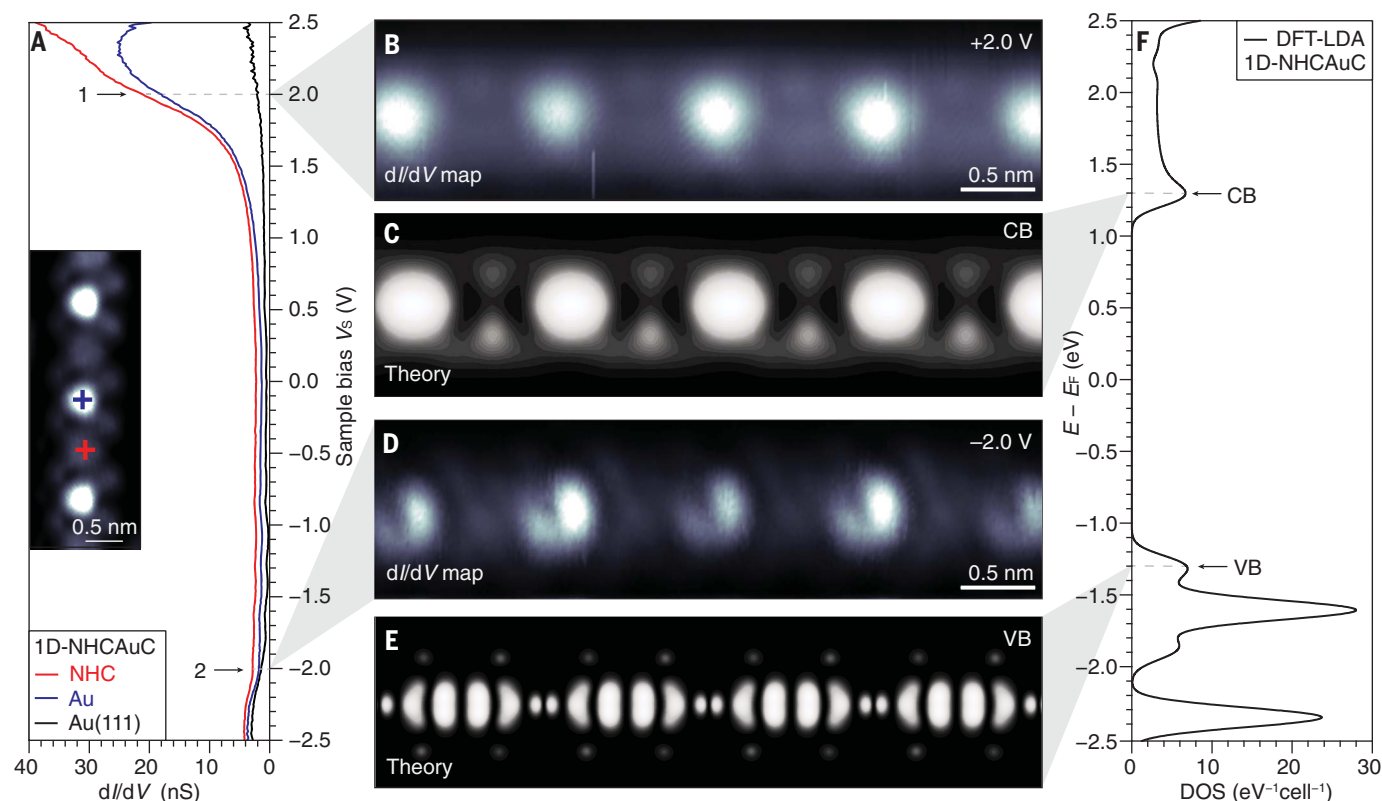
Fig. 3. Electronic structure of 1D-NHCAuC. (**A**) d*I*/d*V* point spectra of 1D-NHCAuC on Au(111) recorded at the positions marked in the inset (V_{ac} = 4 mV, *f* = 533 Hz, CO-functionalized tip). (**B**) Constant-height d*I*/d*V* map of 1D-NHCAuC recorded at a sample voltage bias of V_s = +2.0 V (V_{ac} = 30 mV, *f* = 533 Hz, CO-functionalized tip). (**C**) DFT-LDA calculated LDOS map above freestanding 1D-NHCAuC at the conduction band edge energy. (**D**) Constant-height d*I*/d*V* map of 1D-NHCAuC recorded at a bias of V_s = −2.0 V (V_{ac} = 30 mV, *f* = 533 Hz, CO-functionalized tip). (**E**) DFT-LDA calculated LDOS map above freestanding 1D-NHCAuC at the valence band edge energy. (**F**) DFT-LDA calculated DOS of freestanding 1D-NHCAuC (spectrum broadened by 10 meV Gaussian and shifted up with regard to E_F by 2.94 eV to match the gold p-doping effect). All STM experiments were performed at *T* = 4 K.

lattice. A tight-binding analysis of this 2D model revealed the typical Kagome band structure featuring two Dirac bands crossing the Fermi level (E_F) with an unoccupied flat band at higher energy (*10, 11*).

In situ synthesis of NHC-metal lattices

Using this theoretical approach as a guide, we designed molecular building blocks that would enable the in situ on-surface synthesis of 1D-NHCAuC and 2D-NHCAuKL. We synthesized a linear divalent NHC ligand based on a benzene ring (for 1D-NHCAuC) and a triangular trivalent NHC ligand derived from a triphenylene core (for 2D-NHCAuKL). Figure 2 outlines the synthetic bottom-up approach that gives rise to these low-dimensional carbene architectures on a Au(111) substrate. Inspired by earlier reports detailing the self-assembly and bonding modes of monofunctional NHCs on Au(111) surfaces (*12–23*), we selected two organic salts, 1,3,5,7-tetramethyl-3,7-dihydrobenzo[1,2-d:4,5-d']diimidazole-1,5-diium bis(tetrafluoroborate) (**2**) and 1,3,6,8,11,13-hexamethyl-6,11-dihydro-1H-triphenyleno[2,3-d:6,7-d':10,11-d'']triimidazole-3,8,13-triium tri(tetrafluoroborate) (**3**), as precursors for the on-surface synthesis of low-dimensional

lattices. Organic synthetic procedures that yield analytically pure samples for ultrahigh vacuum (UHV) deposition can be found in the supplementary materials (fig. S2).

To assemble 1D-NHCAuC, we sublimed diimidazolium tetrafluoroborate **2** (the linear chain precursor) in UHV from a Knudsen cell evaporator onto a pristine Au(111) substrate held at 298 K. A subsequent annealing step at 470 K induced the in situ thermal fragmentation of the tetrafluoroborate salt **2** into the neutral bis-NHC-carbene linker (*24–26*). A pair of NHC ligands coordinated to a single shared Au adatom to form the characteristic NHC–Au–NHC junction. Figure 2, B and C, shows representative STM topographic images (*T* = 4 K) of self-assembled 1D-NHCAu chains. The lengths of these chains exhibited considerable spread, ranging from <10 nm in low-density submonolayer samples to >40 nm in samples prepared from monolayers of precursor **2** deposited on Au(111) (fig. S3, A to D). While the growth and relative alignment of 1D-NHCAu chains does not follow the Au(111) herringbone surface reconstruction (fig. S3A), the uniform lateral spacing of oligomers in low-density submonolayer samples hints at a

strong Coulombic repulsion between charged 1D-NHCAu oligomers (fig. S3, E to G) (*27, 28*).

An x-ray photoelectron spectroscopy (XPS) survey performed on a dense monolayer of 1D-NHCAuC on Au(111) showed spectral signatures for carbon, nitrogen, and gold (fig. S4A). The absence of signals at the boron and fluorine edge, the elements associated with the tetrafluoroborate counter-anion in **2**, suggests a clean decomposition of the NHC precursor followed by traceless desorption of the fragmentation products during surface growth (fig. S4C). High-resolution XPS (HR-XPS) in the spectral windows associated with the binding energy of C 1s (fig. S4D) and Au 4f (fig. S4E) states showed characteristic shoulders at 286.6 and 85.1 eV, respectively. These features have previously been interpreted as signatures of NHC–Au bonds adsorbed parallel to the Au(111) surface (*21, 29*). STM topographic imaging of samples subjected to XPS revealed that even prolonged exposure of 1D-NHCAuC to air and moisture for 48 hours did not lead to a noticeable degradation of the NHC–Au–NHC chains (fig. S4B).

A closer inspection of STM images (Fig. 2C) revealed a strictly linear configuration of

1D-NHCAu chains. As coverage increased, these structures assembled into locally aligned domains (~100 nm^2). Bright protrusions within the chains coincided with the positions of the NHC–Au–NHC junctions, separated by an average interjunction distance of ~1 nm. We were unable to fully resolve the atomic structure of the corrugated 1D-NHCAuC backbone with BRSTM imaging, but the position and spacing of Au atoms, the protruding methyl substituents on either side of the NHC ligand, and the central benzene ring (introduced as an organic spacer) were prominently featured in the BRSTM images of Fig. 2D and fig. S5. The bright regions in Fig. 2D and the constant current STM height profile variations of $\Delta z \sim 70$ pm recorded across NHC–Au–NHC junctions (fig. S6, A and B) suggested a bonding between NHC ligands and Au adatoms rather than an alternative bonding mode involving atoms in the Au(111) surface.

To further corroborate the structural integrity of NHC–Au chains, an STM tip manipulation experiment was conducted to transfer the in situ formed 1D-NHCAuC onto an island of monolayer potassium bromide (KBr) codeposited on Au(111). The resulting STM topographic image (fig. S7) of the 1D-NHCAuC on a KBr island indicated that the Au atoms remained firmly bound to the NHC ligands and moved as a single unit even when lifted off the Au surface. The subtle differences in the STM topography of NHC–Au–NHC junctions on Au(111) and KBr can be attributed to changes in the adsorption geometry and interaction with the underlying substrate. The broad applicability of this growth strategy for 1D NHC-metal chains was further highlighted by the extension of this approach to Ag(111) surfaces. The formation of 1D-NHCAg chains up to 30 nm in length was observed after submonolayer deposition and the on-surface synthesis protocol for **2** on Ag(111), as detailed in the supplementary materials (fig. S8).

Building on the in situ synthesis of 1D chains, the triimidiazolium tetrafluoroborate **3**, a precursor featuring the D$_{3h}$ symmetry of a triphenylene core, was applied to the synthesis of the corresponding 2D-NHCAuKL. The exceptionally low vapor pressure of the organic tetrafluoroborate salt precluded its sublimation and required us to rely on a direct contact transfer (DCT) protocol to deposit **3** onto a clean Au(111) substrate (30–32). Subsequent annealing of the molecule-decorated surface at $T = 400$ K initiated the self-assembly of the 2D-NHCAuKL (Fig. 2E). Again, Au atoms were extracted from the Au(111) substrate to form NHC–Au–NHC junctions and coordinated to the trivalent organic NHC linkers to form 2D Kagome lattices.

Topographic STM images in Fig. 2F and fig. S9A provide large-area scans of a low-density submonolayer sample featuring isolated patches

of 2D-NHCAuKL after the DCT and annealing steps. A close-up STM topographic image (Fig. 2G and fig. S9B) reveals bright protrusions at the center of each edge within the rings of the Kagome lattice. These bright spots correspond to the positions of the NHC–Au–NHC junctions, whereas slightly dimmer contrast is observed at the threefold vertices associated with the triphenylene linkers. The Fourier transform (FT) of the topographic STM image of Fig. 2G (Fig. 2H) exhibits distinct points corresponding to the 2D-NHCAuKL lattice structure. Dashed lines connect the reciprocal lattice vectors expected for 2D-NHCAuKL.

Although six-membered rings are prevalent in the 2D-NHCAuKL, the flexibility of the C–Au–C bond angle in the NHC–Au–NHC junction accommodated the formation of rings of varying sizes. This structural plasticity led to the formation of defects containing five- and seven-membered rings, as well as rare examples of four- and eight-membered rings. BRSTM images of 2D-NHCAuKL (Fig. 2I and fig. S9, C and D) confirm the position of gold adatoms, the methyl groups of the NHC ligands, and triphenylene linkers within the lattice structure. The characteristic bright spots are consistent with the positions of the NHC–Au–NHC junctions, as well as the extracted height profile variations ($\Delta z \sim 60$ pm; fig. S6, C and D). These imaging results suggest that 2D-NHCAuKL has a bonding mode similar to 1D-NHCAuC involving the formation of a linear complex of two NHC ligands coordinated to a single Au-adatom.

To further compare the experimental STM observations of in situ synthesized 1D-NHCAuC and 2D-NHCAuKL structures with the expected NHC–Au–NHC bonding mode, we performed DFT simulations of the 1D and 2D surface structures including the Au(111) substrate (fig. S10). Top-down (fig. S10, A and C) and side-on (fig. S10, B and D) projections of simulated 1D-NHCAuC and 2D-NHCAuKL lattices on Au(111) showed a pronounced corrugation in which the bonding Au adatoms in NHC–Au–NHC junctions were lifted ~3.4 Å above the plane of the Au(111) surface. The theory is in qualitative agreement with the height profiles extracted from STM topographic imaging that show Au atoms in 1D-NHCAuC protruding slightly higher from the NHC–Au–NHC junction than the corresponding atoms in 2D-NHCAuKL (fig. S6).

Scanning tunneling spectroscopy of NHC–Au lattices

We used STS to explore how the frontier states associated with NHC–Au–NHC bonding modes contributed to the electronic structure of 1D-NHCAuC and 2D-NHCAuKL. Figure 3A shows typical dI/dV point spectra recorded on a 1D-NHCAuC at the positions marked in the inset [dI/dV spectroscopy reflects the local density of states (LDOS) beneath the STM tip]. The onset of a peak at $V_s = +2.0$ V (state 1) and a smaller

feature at $V_s = -2.0$ V (state 2) can be seen in differential conductance spectra recorded above both the Au atom and the NHC linker. The energy range spanning -2.0 V $< V_s <$ $+2.0$ V remained featureless, suggesting that 1D-NHCAuC on Au(111) is a wide-gap semiconductor. A series of dI/dV maps recorded at biases of -2.5 V $< V_s <$ $+2.3$ V are provided in the supplementary materials (fig. S11) and show a characteristic background signal associated with the corrugation along the main axis of 1D-NHCAu chains (see figs. S6, S10, and S12). The characteristic pattern of bright circular features resulting from a local modulation of the STM tip-sample distance in dI/dV maps coincides with the position of the Au atoms and could even be seen at $V_s = 0.0$ V, well within the semiconducting gap. dI/dV mapping at $V_s = +2.0$ V revealed the spatial distribution of the LDOS corresponding to state 1 (Fig. 3B). Most prominent is a spherical feature at the position of the Au atoms, flanked on either side by two smaller lobes associated with the benzene ring in the NHC linker. dI/dV maps recorded at $V_s = -2.0$ V revealed the LDOS corresponding to state 2 (Fig. 3D). This negative bias state showed a nodal feature at the position of the Au atom reminiscent of the NAO contributions from Au $5d_{xz}$ to the β-HOMO and α-HOMO−1 orbitals in NHC–Au–NHC dimer **1** (fig. S1).

The STS characterization of 2D-NHCAuKL is shown in Fig. 4. dI/dV point spectra were recorded at the positions marked by crosses in the inset image (Fig. 4A). The onset of a peak at $V_s = +1.8$ V (state 3) and a smaller signature at $V_s = -2.0$ V (state 4) bracket a featureless energy range consistent with a wide-gap semiconductor. dI/dV maps recorded across a wide bias range show a familiar pattern of brighter contrast at the position of the Au atoms resulting from a local corrugation of the 2D-NHCAuKL (see figs. S6, S10, and S13). Against this background, dI/dV maps recorded at $V_s = +1.8$ V (state 3) and $V_s = -2.0$ V (state 4) show two distinctive nodal patterns associated with the triphenylene core of the NHC linker (Fig. 4, B and C). dI/dV maps at energies corresponding to state 4 further reveal the faint signature of a node at the position of the Au atoms suggestive of NAO contributions from Au $5d_{xz}$ orbitals.

Ab initio calculations of NHC–Au lattices

To interpret our experimental STS spectra, we analyzed the local electronic structure of NHC–Au lattices using ab initio DFT. Figure 5A shows the calculated DFT band structure for freestanding charge-neutral 1D-NHCAuC using the local density approximation (LDA) for the exchange-correlation potential. A single band crosses E_F, which suggests that an isolated molecular chain should be metallic. A small energy gap of 0.15 eV lies above the half-filled metallic band whereas a much larger gap of 2.5 eV separated the bottom of the metallic
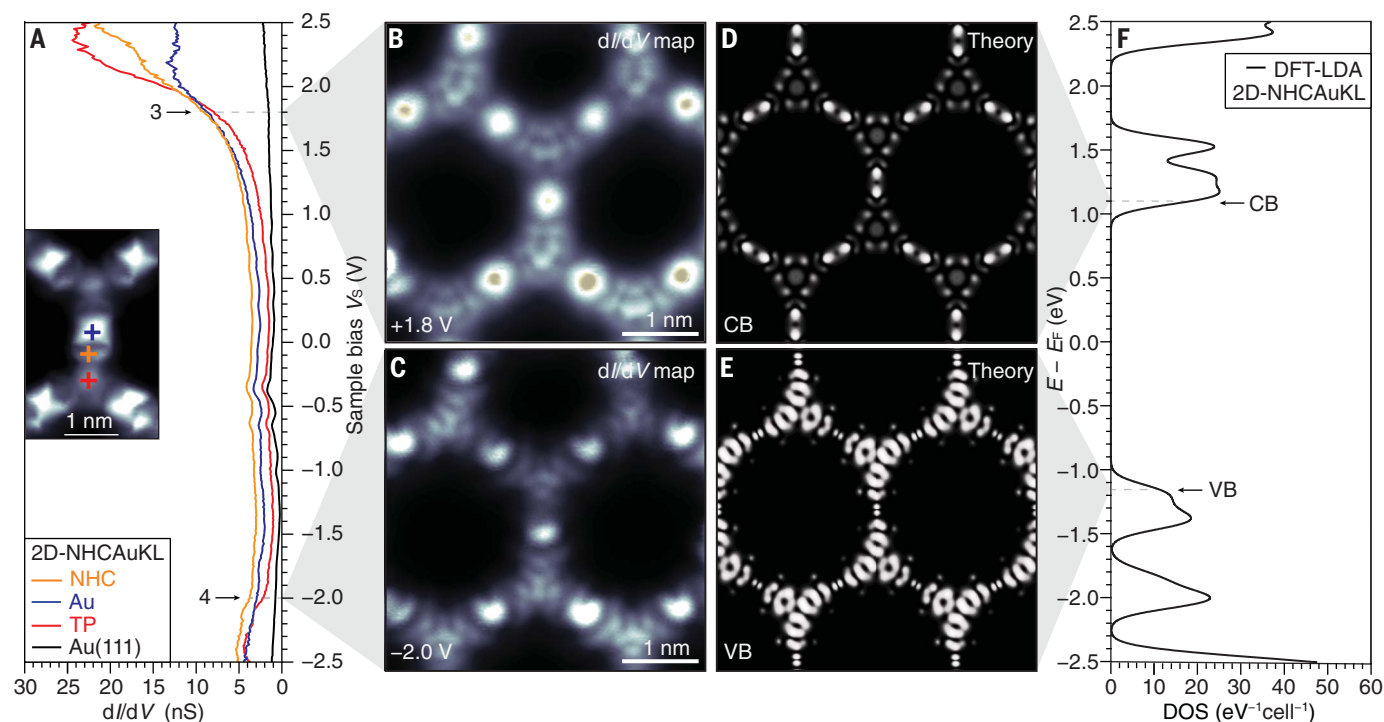
Fig. 4. Electronic structure of 2D-NHCAuKL. (A) dI/dV point spectra of 2D-NHCAuKL on Au(111) recorded at the positions marked in the inset (V_{ac} = 4 mV, f = 533 Hz, CO-functionalized tip). **(B)** Constant-height dI/dV map of 2D-NHCAuKL recorded at a sample voltage bias of V_s = +1.8 V (V_{ac} = 30 mV, f = 533 Hz, CO-functionalized tip; light-yellow circles represent the tunneling current signal exceeding 100 nA in STM measurement). **(C)** Constant-height dI/dV map of 2D-NHCAuKL recorded at a bias of V_s = –2.0 V (V_{ac} = 30 mV, f = 533 Hz, CO-functionalized tip). **(D)** DFT-LDA calculated LDOS map above freestanding 2D-NHCAuKL at the conduction band edge energy. **(E)** DFT-LDA calculated LDOS map above freestanding 2D-NHCAuKL at the valence band edge energy. **(F)** DFT-LDA calculated DOS of freestanding 2D-NHCAuKL (spectrum broadened by 10 meV Gaussian and shifted up with regard to E_F by 2.62 eV to match the gold p-doping effect). All STM experiments were performed at T = 4 K.

band from a dispersive low-lying occupied state. Using a tight-binding approximation with a single hopping parameter (t_{1D}) between C–Au–C π-bonding states, we could fit the metallic band with t_{1D} = 229 meV and an on-site energy ε = 0.136 eV (Fig. 5B, red dashed line). Figure 5, C and D, shows the DFT-LDA wave function isosurface, top-down and side-on view, respectively, and highlights a large contribution from the C–Au–C bonding molecular orbital to the metallic band.

DFT calculations further reveal an unusually small work function $\Phi_{1D-NHCAuC}$ = 1.9 eV for the freestanding 1D-NHCAuC that can be attributed to the high energy of the SOMO orbital associated with the NHC–Au–NHC junction. The work function of 1D-NHCAuC is much smaller than that of the underlying gold metal (Φ_{Au} ≈ 5.3 eV) (*33*). Charge transfer from the NHC–Au lattice to the Au substrate is thus expected to completely deplete the charge carriers in the metallic band, pushing its lower band edge above E_F and resulting in the sizable bandgap experimentally observed for 1D-NHCAuC on Au(111). This charging effect is consistent with the uniform separation of 1D-NHCAuC oligomers by Coulombic repulsion observed in topographic STM images recorded on

submonolayer 1D-NHCAuC samples on Au(111) (fig. S3, E to G).

Figure 3F shows the calculated DFT-LDA DOS adjusted for an expected 2.94 eV shift of the 1D-NHCAuC band structure on gold from charge transfer. A broad conduction band (CB) peak at $E - E_F$ = +1.3 eV corresponds reasonably well with the experimental dI/dV point spectra for 1D-NHCAuC (Fig. 3A). A projection of the calculated LDOS at the bottom of the CB (Fig. 3C) faithfully reproduced the orbital patterns observed in experimental dI/dV maps recorded at V_s = +2.0 V (state 1, Fig. 3B) and provided strong evidence that this state primarily consisted of the C–Au–C π-bonding state (Fig. 5, C and D). In contrast, the theoretical LDOS projected at the edge of the valence band (VB) at $E - E_F$ = –1.3 eV showed a nodal plane at the position of the Au atom, thus reflecting contributions from the Au $5d_{xz}$ NAO (Fig. 3E). Experimental dI/dV maps recorded at V_s = –2.0 V (state 2) show similar nodal structure, albeit with markedly higher intensity on the Au atoms protruding Δz ~ 70 pm above the plane of the NHC linkers (Fig. 3D).

We applied a similar theoretical analysis to explore the contributions of NHC–Au–NHC junction states to the electronic structure of

the 2D Kagome lattice. Figure 5E shows the band structure of freestanding charge-neutral 2D-NHCAuKL calculated with DFT-LDA. A pair of dispersive half-filled metallic bands crosses the E_F, flanked at higher energy by an unoccupied Kagome flat-band and separated from the next lower-energy occupied bands by a sizable energy separation (ΔE = 2.25 eV). Figure 5F shows that the three characteristic Kagome bands at E_F can be fit by using a simple tight-binding model with a single hopping parameter t_{2D} = 47 meV and an on-site energy ε = 0.015 eV to describe the 2D bands formed out of C–Au–C π-bonding orbitals. The DFT-LDA wave function isosurface for the states contributing to the Kagome bands crossing E_F is shown in Fig. 5, G and H. The DFT-LDA calculations also predict a small work function of $\Phi_{2D-NHCAuKL}$ = 2.3 eV for 2D-NHCAuKL.

Similar to the 1D case, electron transfer between the isolated metallic Kagome bands and the gold substrate is expected to empty the 2D-NHCAuKL metallic band and shift it up in energy relative to the gold E_F, giving rise to the experimentally observed large semiconducting bandgap. To account for this p-doping effect, the calculated 2D-NHCAuKL DOS was shifted by 2.62 eV relative to E_F in Fig. 4F. The peak at
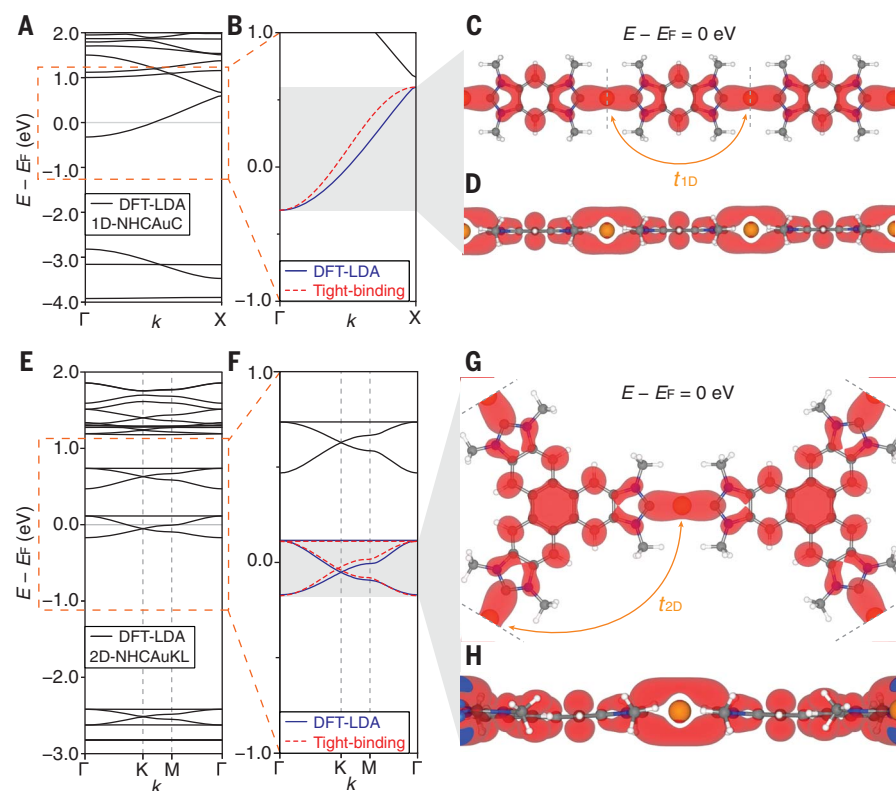
Fig. 5. Band structures of NHC–Au lattices. (**A**) DFT-LDA band structure of freestanding 1D-NHCAuC. (**B**) Tight-binding fit (red) to the DFT-LDA metallic band of 1D-NHCAuC (blue). (**C** and **D**) DFT-LDA calculated wave function isosurface of the states near $E - E_F = 0$ (isosurface level: 9×10^{-4}) in freestanding 1D-NHCAuC. The C–Au–C π-bonding states on the NHC–Au–NHC junctions are visualized in (C) top-down and (D) side-view projections. (**E**) DFT-LDA band structure of freestanding 2D-NHCAuKL. (**F**) Tight-binding fit (red) to the DFT-LDA Kagome bands of 2D-NHCAuKL (blue). (**G** and **H**) DFT-LDA calculated wave function isosurface of the states near $E - E_F = 0$ (isosurface level: 4×10^{-5}) in freestanding 1D-NHCAuC. The C–Au–C π-bonding states on the NHC–Au–NHC junctions are visualized in (G) top-down and (H) side-view projections.

$E - E_F = +1.1$ eV represents the bottom of the CB and corresponds to state 3 in the experimental dI/dV point spectra for 2D-NHCAuKL (Fig. 4A). Projections of the theoretical LDOS at $E - E_F = +1.1$ eV (Fig. 4D) correspond reasonably well to the orbital patterns in the experimental dI/dV maps recorded at $V_s = +1.8$ V (Fig. 4B), showing that state 3 is primarily composed of contributions from the localized C–Au–C π-bonding orbital to the dispersive Kagome bands. The theoretical LDOS of states at the edge of the VB at $E - E_F = -1.1$ eV shows the signature of nodal planes arising from Au $5d_{xz}$ NAOs (Fig. 4E). This characteristic nodal pattern corresponds reasonably well to the experimental dI/dV maps recorded at $V_s = -2.0$ V (state 4, Fig. 4C).

To investigate the electronic behavior of NHC–Au lattices on Au(111) surfaces, we analyzed the electronic structure of the DFT simulated 1D-NHCAuC and 2D-NHCAuKL including the Au(111) substrate (figs. S10, S12A, and S13A). Figures S12B and S13B illustrate the DFT-LDA projected wave function isosurface for the CBs of 1D-NHCAuC and 2D-NHCAuKL, respectively,

indicating a strong hybridization between the C–Au–C π-bonding states and the gold substrate. In contrast, the interaction between the VBs and Au(111) substrate appears to be weaker (figs. S12C and S13C). The projected density of state (PDOS) analysis reveals that the band edge of 1D-NHCAuC and 2D-NHCAuKL is elevated above E_F after the electron transfer from the metallic bands of the freestanding NHC–Au lattices to the Au(111) substrate (figs. S12D and S13D).

Discussion

We have presented a robust methodology for designing and fabricating extended, low-dimensional NHC lattices with intrinsic metallic properties by strategically designing molecular precursors for bottom-up in situ synthesis. By deterministically engineering the frontier orbitals of the NHC–Au junctions, we have successfully constructed 1D chains (1D-NHCAuC) and 2D Kagome lattices (2D-NHCAuKL). These structures feature electronic signatures stemming from a distinctive NHC–metal bonding mode. The unusually high energy associated with the SOMO formed by C–Au–C

π-bonding molecular states leads to a reduced work function in these low-dimensional crystals that is comparable to bulk alkali metals (Φ_{Li} = +2.93 eV; Φ_{Na} = +2.36 eV; Φ_K = +2.29 eV; Φ_{Rb} = +2.26 eV; Φ_{Cs} = +1.95 eV) (*34*). Our highly modular bottom-up approach not only gives access to exceptionally low work function metals but also creates future opportunities for exploring electronic and magnetic phenomena emerging from low-dimensional NHC–transition metal networks.

REFERENCES AND NOTES

1. M. N. Hopkinson, C. Richter, M. Schedler, F. Glorius, *Nature* **510**, 485–496 (2014).
2. C. A. Smith *et al.*, *Chem. Rev.* **119**, 4986–5056 (2019).
3. M. Koy, P. Bellotti, M. Das, F. Glorius, *Nat. Catal.* **4**, 352–363 (2021).
4. D. J. Nelson, S. P. Nolan, *Chem. Soc. Rev.* **42**, 6723–6753 (2013).
5. D. Nemcsok, K. Wichmann, G. Frenking, *Organometallics* **23**, 3640–3646 (2004).
6. E. D. Glendening, C. R. Landis, F. Weinhold, *J. Comput. Chem.* **34**, 1429–1437 (2013).
7. T. Lu, F. Chen, *J. Comput. Chem.* **33**, 580–592 (2012).
8. M. J. Frisch *et al.*, Gaussian 16 Revision C.01 (Gaussian, Inc., 2016).
9. A. J. Heeger, S. Kivelson, J. R. Schrieffer, W. P. Su, *Rev. Mod. Phys.* **60**, 781–850 (1988).
10. W. Jiang, X. Ni, F. Liu, *Acc. Chem. Res.* **54**, 416–426 (2021).
11. M. A. Springer, T. J. Liu, A. Kuc, T. Heine, *Chem. Soc. Rev.* **49**, 2007–2019 (2020).
12. C. M. Crudden *et al.*, *Nat. Chem.* **6**, 409–414 (2014).
13. C. R. Larrea *et al.*, *ChemPhysChem* **18**, 3536–3539 (2017).
14. L. Jiang *et al.*, *Chem. Sci.* **8**, 8301–8308 (2017).
15. G. Wang *et al.*, *Nat. Chem.* **9**, 152–156 (2017).
16. Y. Zeng, T. Zhang, M. R. Narouz, C. M. Crudden, P. H. McBreen, *Chem. Commun.* **54**, 12527–12530 (2018).
17. A. Bakker *et al.*, *J. Am. Chem. Soc.* **140**, 11889–11892 (2018).
18. S. Amirjalayer, A. Bakker, M. Freitag, F. Glorius, H. Fuchs, *Angew. Chem. Int. Ed.* **59**, 21230–21235 (2020).
19. P. Knecht *et al.*, *J. Am. Chem. Soc.* **143**, 4433–4439 (2021).
20. M. Franz *et al.*, *Nat. Chem.* **13**, 828–835 (2021).
21. A. Inayeh *et al.*, *Nat. Commun.* **12**, 4034 (2021).
22. J. J. Navarro *et al.*, *Angew. Chem. Int. Ed.* **61**, e202202127 (2022).
23. J. Ren *et al.*, *Nat. Chem.* **15**, 1737–1744 (2023).
24. U. Jung *et al.*, *Langmuir* **27**, 5899–5908 (2011).
25. S. Snegir *et al.*, *Phys. Chem. Chem. Phys.* **23**, 9930–9937 (2021).
26. K. L. Syres, R. G. Jones, *Langmuir* **31**, 9799–9808 (2015).
27. E. C. H. Wen *et al.*, *J. Am. Chem. Soc.* **144**, 13696–13703 (2022).
28. F. Liou *et al.*, *Adv. Mater.* **35**, e2300542 (2023).
29. G. Lovat *et al.*, *Chem. Sci.* **10**, 930–935 (2018).
30. J. D. Teeter *et al.*, *Nanoscale* **9**, 18835–18844 (2017).
31. P. H. Jacobse *et al.*, *Sci. Adv.* **7**, eabl5892 (2021).
32. P. M. Albrecht, J. W. Lyding, *Appl. Phys. Lett.* **83**, 5029–5031 (2003).
33. W. M. H. Sachtler, G. J. H. Dorgelo, A. A. Holscher, *Surf. Sci.* **5**, 221–229 (1966).
34. J. Hölzl, F. K. Schulte, H. Wagner, *Solid Surface Physics*, vol. 85 of Springer Tracts in Modern Physics (Springer-Verlag, 1979).
35. P. Giannozzi *et al.*, *J. Phys. Condens. Matter* **21**, 395502 (2009).
36. QUANTUM ESPRESSO; https://www.quantum-espresso.org/.
37. Python Tight Binding (PythTB); https://www.physics.rutgers.edu/pythtb/.

Author contributions: Conceptualization: B.Q., Z.W., and F.R.F. Investigation: B.Q., Z.W., J.J., and Z.Z. Funding acquisition: F.R.F., M.F.C., S.G.L., and A.N.A. Project administration: F.R.F. Supervision: F.R.F., M.F.C., S.G.L., and A.N.A. Writing – original draft: B.Q. and F.R.F. Writing – review & editing: B.Q., Z.W., J.J., Z.Z., P.H.J., J.L., X.L., F.L., A.N.A., S.G.L., M.F.C., and F.R.F. **Competing interests:** The authors declare that they have no competing interests. **Data and materials availability:** The DFT code and pseudopotentials can be downloaded from the Quantum Espresso website (*35, 36*). For this study, we used version 6.7 for the DFT-LDA calculations. The tight-binding simulation code can be downloaded from the PythTB website (*37*). For this study, we used version 1.8.0 for the tight-binding fitting. All data are available in the main text or the supplementary materials.

SUPPLEMENTARY MATERIALS

science.org/doi/10.1126/science.adm9814
Materials and Methods
Figs. S1 to S13
References (*38–48*)